



OPEN

SUBJECT AREAS:

INORGANIC LEDs  
NANOPHOTONICS AND  
PLASMONICSReceived  
26 November 2013Accepted  
27 February 2014Published  
14 March 2014Correspondence and  
requests for materials  
should be addressed to  
K.H. (k\_huang@xmu.  
edu.cn) or J.C.L.  
(jinchaili@xmu.edu.cn)

# Top- and bottom-emission-enhanced electroluminescence of deep-UV light-emitting diodes induced by localised surface plasmons

Kai Huang, Na Gao, Chunzi Wang, Xue Chen, Jinchai Li, Shuping Li, Xu Yang &amp; Junyong Kang

Department of Physics, Fujian Provincial Key Laboratory of Semiconductor Materials and Application, Xiamen University, Xiamen, 361005, P. R. China.

We report localised-surface-plasmon (LSP) enhanced deep-ultraviolet light-emitting diodes (deep-UV LEDs) using Al nanoparticles for LSP coupling. Polygonal Al nanoparticles were fabricated on the top surfaces of the deep-UV LEDs using the oblique-angle deposition method. Both the top- and bottom-emission electroluminescence of deep-UV LEDs with 279 nm multiple-quantum-well emissions can be effectively enhanced by the coupling with the LSP generated in the Al nanoparticles. The primary bottom-emission wavelength is longer than the primary top-emission wavelength. This difference in wavelength can be attributed to the substrate-induced Fano resonance effect. For resonance modes with shorter wavelengths, the radiation fraction directed back into the LEDs is largest in the direction that is nearly parallel to the surface of the device and results in total reflection and re-absorption in the LEDs.

Semiconductor deep-ultraviolet (deep-UV) light sources based on III-nitride light-emitting diodes (LEDs) have been intensively investigated because of their potential applications, including air and water purification, germicidal and biomedical instrumentation systems, and ophthalmic surgery tools<sup>1–3</sup>. Although researchers have reported deep-UV LEDs at a wavelength of 280 nm with IQEs as high as 70%<sup>4</sup>, the adoption of deep-UV LED technology is still hindered by the relatively low efficiency of these devices, which are limited by low light-extraction efficiency (LEE) caused by total internal reflection and dominant TM-polarised spontaneous emission<sup>5–7</sup>.

To improve the LEE of LEDs with emission wavelengths longer than 300 nm, numerous approaches have been developed, such as photonic-crystal LEDs<sup>8–10</sup>, patterned substrates<sup>11,12</sup>, and integrated microlens arrays<sup>13–15</sup>. However, these methods can lead to a reduction in only the total internal reflection caused by the high refractive index. For deep-UV LEDs using  $\text{Al}_x\text{Ga}_{1-x}\text{N}$  ( $x > 0.25$ ) as active layers, the most dominant emission will be photons with polarisation parallel to the crystal axis ( $\text{E} \parallel c$ ), implying that deep-UV photons will propagate parallel to the active layers of LEDs<sup>16,17</sup>. Thus, to improve the LEE, those surface modification methods described above are less effective for the AlGaIn based deep-UV LEDs than for LEDs with longer emission wavelengths. Recently, we have reported a surface-plasmon-enhanced (SP-enhanced) deep-UV LED structure using a thin layer of aluminium to enhance the LEE of deep-UV LEDs<sup>18</sup>. Unlike the conventional SP-quantum well (SP-QW) coupling of GaN-based LEDs in the visible region<sup>19,20</sup>, the LEE of LEDs is enhanced by drawing TM-polarised spontaneous emission from the devices. However, this structure is not the optimal structure for the enhancement of the LEE of deep-UV LEDs. For the acquisition of high-LEE deep-UV LEDs using the SP-coupling method, localised surface plasmons (LSPs) offer greater advantages than SPs. The first reason for the greater utility of LSPs in these devices is that the thin aluminium layer can only couple to a TM wave parallel to the surface of the device. For a TE wave propagating in the direction parallel to the device surface, SP coupling does not occur. Meanwhile, for a wave in the escape zone generated in the active layer, photons must penetrate through the aluminium layer and then be emitted from the top surface of the device. When the thickness of the aluminium layer is 6 nm, the photon energy will be reduced to approximately 40% of its initial energy. The second reason is that SPs can only effectively couple with photons and radiate into photons when their momentum is properly matched with that of the photons. Thus, the surfaces of the LEDs must not be perfectly flat<sup>21</sup>. However, a flatter top surface generally indicates a higher IQE because of the relatively low density of crystal defects. It is well known that  $\eta_{EQE} = \eta_{IQE} \times \eta_{LEE}$ .



Therefore, it is difficult to fabricate deep-UV LEDs of high external quantum efficiency using a structure with a thin aluminium layer for SP coupling.

In comparison with SP-coupling LEDs, LSP-coupling LEDs offer considerable advantages. First, the LSP mode can effectively couple to TE waves, TM waves and waves perpendicular to the device surface. Second, the LSP mode has a broad momentum spectrum and can easily match the momentum of all photons generated in the active layer of LEDs. It can therefore couple to photons and radiate photons more effectively. Third, the study of Chuang *et al.* has demonstrated that LSP coupling can be more effective than SPP coupling in emission enhancement because the latter coupling has a higher dissipation rate near its resonance energy<sup>22</sup>. However, for the relatively high refractive index of GaN-based materials, aluminium nanoparticles (NPs) of relatively small size that can generate LSPs when coupled to deep-UV emission must be fabricated on the LED structures<sup>23,24</sup>.

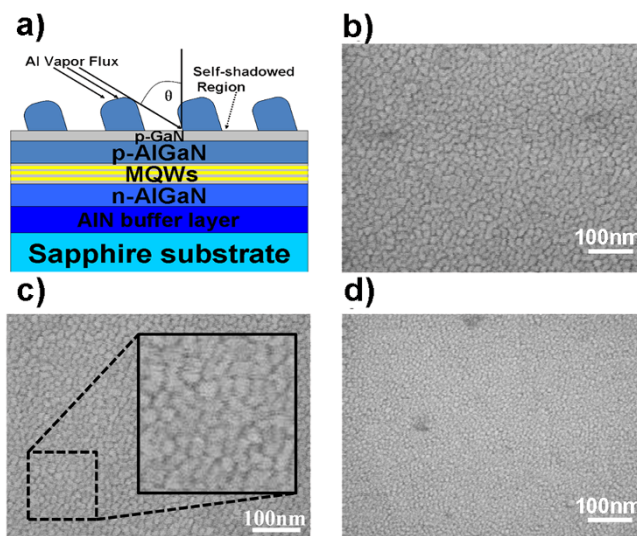
Because metal Al is very easily oxidised in air, the resulting native oxide layer will prevent the surface migration of Al atoms on the substrate; thus, the annealing procedure that is generally used to fabricate self-assembling noble-metal NPs cannot be applied for fabricating Al NP arrays. The fabrication of Al nanostructures has been reported using extreme-ultraviolet (EUV) interference lithography<sup>25</sup> and nanosphere lithography<sup>26</sup>. However, these methods are either expensive or incapable of producing high-density Al NPs. It has been reported that the oblique-angle deposition method can be used to fabricate NPs of controllable feature size and density by varying the deposition angle<sup>27</sup>. In this manner, additional photolithography and annealing steps for nanoscale patterning can be eliminated.

In this paper, we report the implementation of an LSP-enhanced deep-UV LED using Al nanoparticles (NPs) fabricated on top of the LED for LSP coupling. Small, size- and density-controlled Al NPs were fabricated using the oblique-angle deposition method. Photoluminescence (PL) measurements clearly demonstrated that the LEE of such deep-UV LEDs can be enhanced by the coupling of light waves to the LSPs generated in the Al NPs. For LSP-enhanced deep-UV LEDs with Al NPs deposited at a 60° angle, a maximum 10-fold top-emission (epitaxial-layer side) electroluminescence (EL) enhancement at a wavelength of 268 nm and a maximum 2.8-fold bottom-emission (sapphire-substrate side) EL enhancement at a wavelength of 291 nm were achieved. The difference in the top- and bottom-emission wavelengths can be attributed to the substrate-induced Fano resonance effect of the Al nanoparticles<sup>28–30</sup>. The bottom-emission enhancement of the deep-UV LEDs was then optimised using Al NPs deposited at a 75° angle; a maximum 5.1-fold bottom-emission EL enhancement at a wavelength of 287 nm was achieved. The bottom-emission peak-intensity-enhancement ratio increased from 1.36 to 2.75 when the deposition angle was increased from 60° to 75°.

## Results

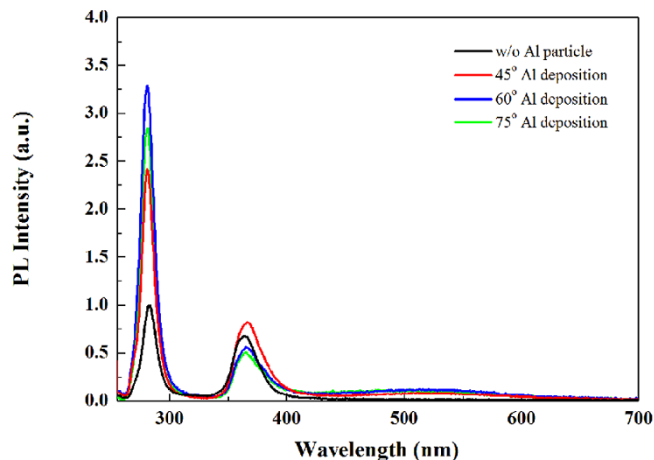
Figure 1a shows a schematic diagram of the deposition of Al NPs on deep-UV LEDs. The Al NPs were deposited directly onto the top surfaces of the complete structural deep-UV LEDs using the oblique-angle deposition method. Top-view SEM images of Al NP arrays of different feature sizes are presented in Fig. 1b–d. The NP arrays were obtained via the deposition of 6 nm Al on a complete structural deep-UV LED at angles of b) 45°, c) 60° and d) 75°. It is evident that the size of such Al NPs can be controlled by varying the deposition angle. The average sizes of the NPs that were deposited at 45°, 60° and 75° angles were approximately 22, 16 and 11 nm, respectively. The densities of the NPs that were deposited at 45°, 60° and 75° were  $2.5 \times 10^{11}$ ,  $5.0 \times 10^{11}$  and  $7.7 \times 10^{11}/\text{cm}^2$ , respectively.

Figure 2 displays the typical room-temperature PL spectra of deep-UV LED samples without Al NPs (sample A) and with Al NPs deposited at 45° (sample B), 60° (sample C) and 75° (sample



**Figure 1 | Schematic illustration and top-view SEM images of the oblique-angle deposition of Al NPs.** (a) Schematic illustration of oblique-angle deposition on complete structural deep-UV LEDs. (b–d) Top-view SEM images of Al NPs deposited on LEDs with deposition angles of 45°, 60° and 75°, respectively.

D). The PL spectrum of sample A contains a strong emission peak at approximately 282 nm and a weak emission peak at 365 nm, which represent the emission of the MQWs and the GaN capping layer, respectively<sup>18</sup>. However, for samples B, C and D, the emission peaks of the MQWs were blueshifted by 2 nm to 280 nm. The spectral blueshift of the samples with Al NPs indicates the existence of an LSP coupling process<sup>31</sup>. The emission peak of sample A at 282 nm is normalised to 1. It is evident that the peak PL intensities of the MQW emission were enhanced to 241%, 329% and 283% for samples B, C and D, respectively. The PL-enhancement ratios of the Al-NP-deposited LEDs are larger than that of planar Al-film-deposited LEDs<sup>18</sup>, thus demonstrating that LSPs are more effective than SPs in LED enhancement. Sample C exhibited the largest enhancement, while the enhancement of sample B was the smallest. When the SEM images of the samples shown in Fig. 1b–d are taken into consideration, it can be deduced that Al NPs of moderate size offer the strongest coupling to the emission of deep-UV LEDs. The size of the NPs affects the PL intensities in two respects: the coupling strength and the radiative recombination rate. Typically, smaller NP sizes will lead



**Figure 2 | Photoluminescence measurements.** PL spectra of deep-UV LED samples without Al NPs (black line) and with Al NPs deposited on the top surfaces at 45° (red line), 60° (blue line) and 75° (green line).

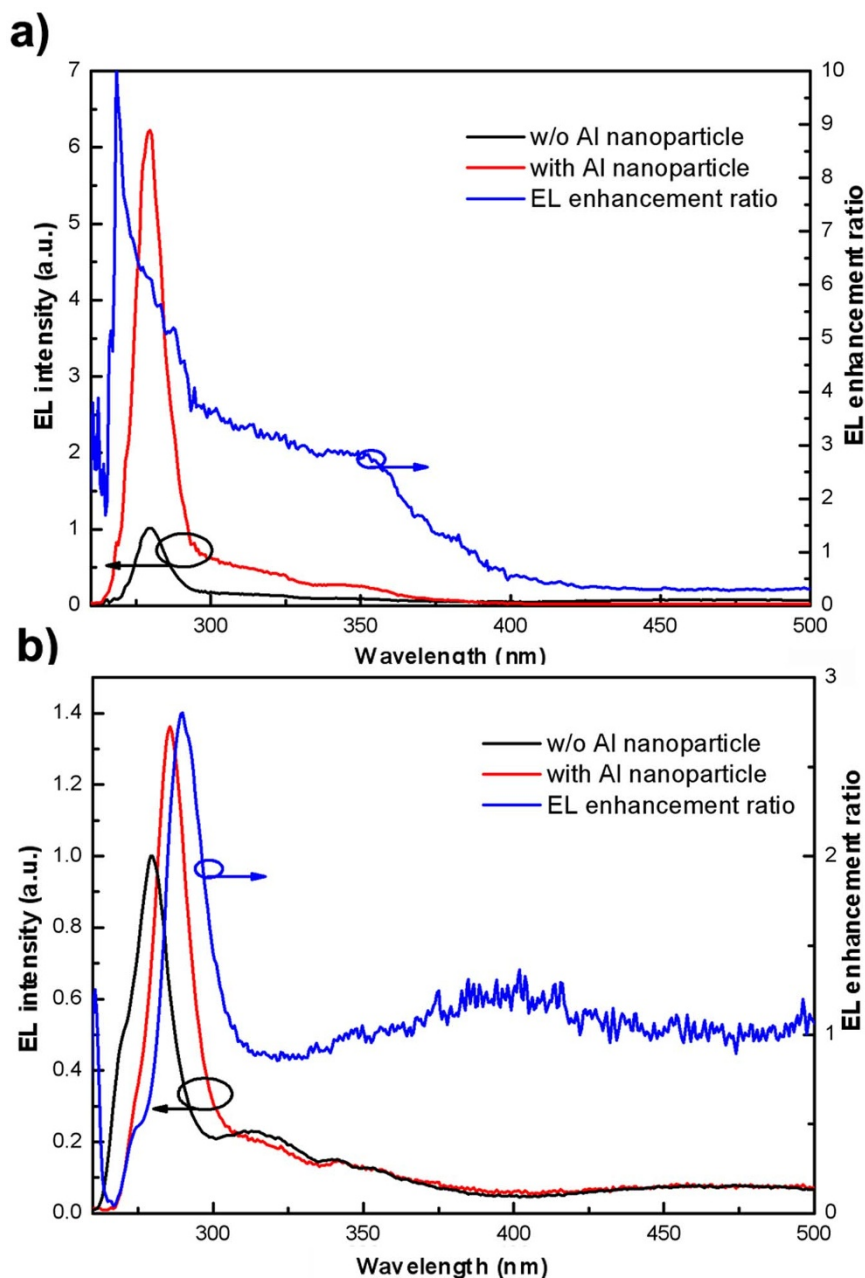


**Figure 3 | Electroluminescence measurements.** (a) Top-emission EL spectra of deep-UV LED samples without Al NPs (black line) and with Al NPs deposited on the top surface at  $60^\circ$  (red line) as well as the enhancement ratio between them (blue line). (b) Bottom-emission EL spectra of deep-UV LED samples without Al NPs (black line) and with Al NPs deposited on the top surface at  $60^\circ$  (red line) as well as the enhancement ratio between them (blue line).

to shorter coupling wavelengths<sup>32</sup>. When the coupling wavelength is closer to the wavelength of the photons generated in the MQWs of the deep-UV LEDs, the coupling strength will be stronger. However, smaller NP sizes will lead to smaller radiative recombination rates<sup>33</sup>. Thus, for deep-UV LEDs with relatively short emission wavelengths, Al NPs of moderate size will produce the strongest PL enhancement.

Because the PL enhancement ratio of sample C was the largest, we measured the EL spectra of sample C. Figure 3a depicts the top-emission EL spectra of sample A and sample C and the enhancement ratio that represents their relative intensities at an injection current of 15 mA. Here, it is apparent that strong emission at a wavelength of approximately 279 nm, representing the band emission of the MQWs, was present in both samples. The emission enhancement caused by the Al NPs is shown as a function of wavelength. The

enhancement ratio increased at shorter wavelengths, with a value of approximately 10 at approximately 268 nm. At the primary emission wavelength, 279 nm, the EL intensity was enhanced to approximately 614%, demonstrating that the top emission of deep-UV LEDs can be enhanced via LSP coupling using Al NPs. The line shape of the enhancement ratio is highly asymmetric, with a steeper slope toward the blue region than toward the red region, indicating that there should be another peak at a longer wavelength (centred at approximately 285 nm). A shoulder centred at approximately 350 nm can also be found in the enhancement-ratio spectrum.

When LSPs are generated via coupling with the light generated in MQWs, they will recombine and generate photons. Photons can be generated at the Al-NP/air interface, leading to top emission. Photons can also be generated at the Al-NP/GaN interface, leading

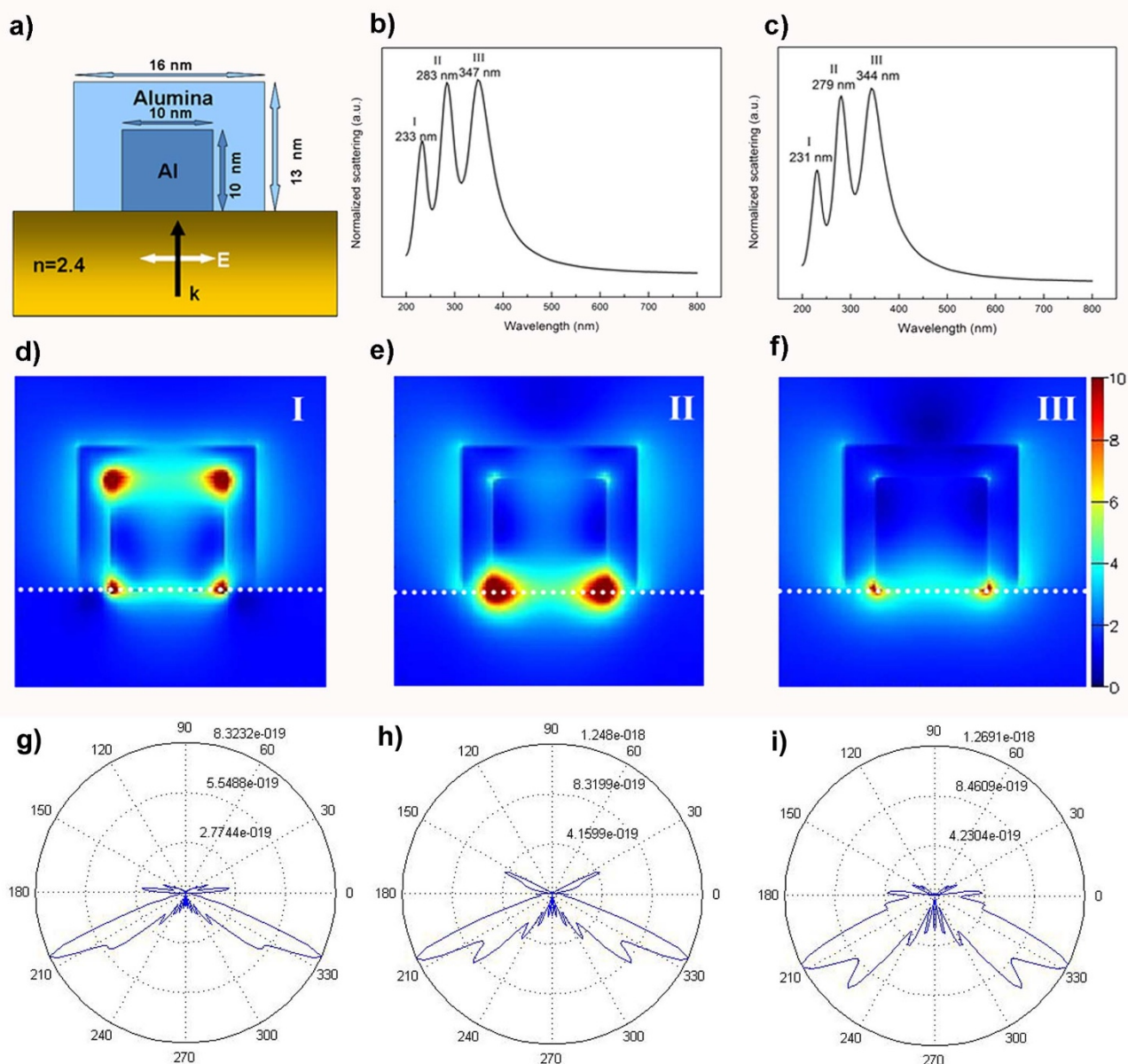


**Figure 4 | FDTD simulations.** (a) Schematic diagram of the structure for the FDTD simulation. (b) Normalised scattering spectrum of the Al/alumina core/shell nanocube depicted in Fig. 4a. (c) Normalised scattering spectrum of a smaller nanocube with an  $8 \times 8 \times 8$  nm Al core within a 3-nm alumina shell on the same substrate. (d–f) Electric-field amplitude for the structure depicted in Fig. 4a at peak I (233 nm), peak II (283 nm) and peak III (347 nm). The incident light is polarised parallel to the cube edge. (g–i) Far-field radiation patterns of peaks I, II and III, respectively.

to bottom emission. Figure 3b shows the bottom-emission EL spectra of sample C and sample A at an injection current of 15 mA. For sample A, the primary emission wavelength remained at 279 nm, while for sample C, the primary emission wavelength underwent a redshift to 286 nm. Unlike the top-emission EL spectra, the enhancement ratio exhibits a relatively symmetric peak at approximately 291 nm with a value of 2.80 and a very weak shoulder at approximately 273 nm. It should be noted that another band centred at approximately 370 nm is also apparent in the enhancement ratio.

To illustrate the physical origin of this phenomenon, in Fig. 4, we present the near-field behaviour calculated using an FDTD simulation. From the inset in Fig. 1c, it can be seen that the shape of the Al NPs was polygonal rather than hemispherical. For simplicity, we chose Al NPs with a cube shape for the FDTD simulation (Fig. 4a). Figure 4b shows the scattering spectra for a 16 nm Al/ $\text{Al}_2\text{O}_3$  core/shell nanocube on a dielectric substrate. There are three peaks in this spectrum at 233 nm (peak I), 283 nm (peak II) and 347 nm (peak

III). Thus, the three peaks/shoulders observed in the top- and bottom-emission enhancement ratios correspond to these calculated peaks. The wavelength difference between the experimental results and the simulation can be attributed to the microstructural differences between the actual Al NPs and the structure used for the simulation. In Figs. 4d–f, the electric-field amplitude distributions outside the cube at the scattering peaks I, II and III are shown. Similar to previously reported results<sup>34</sup>, the blue mode I is oriented predominantly toward the vacuum side, while the red modes II and III are oriented toward the substrate. Zhang *et al.* have proven that such asymmetric plasmon modes are a substrate-induced Fano resonance effect<sup>28</sup>. When the LSPs of resonance modes I, II and III recombine, they produce the far-field radiation patterns shown in Figs. 4g–i. The far-field radiation toward the air is shown in all three figures. Thus, the LSPs associated with modes I, II and III are all evident in the enhancement ratio of the top emission. For the back-emission situation, when the light is generated by the recombination of the LSPs of

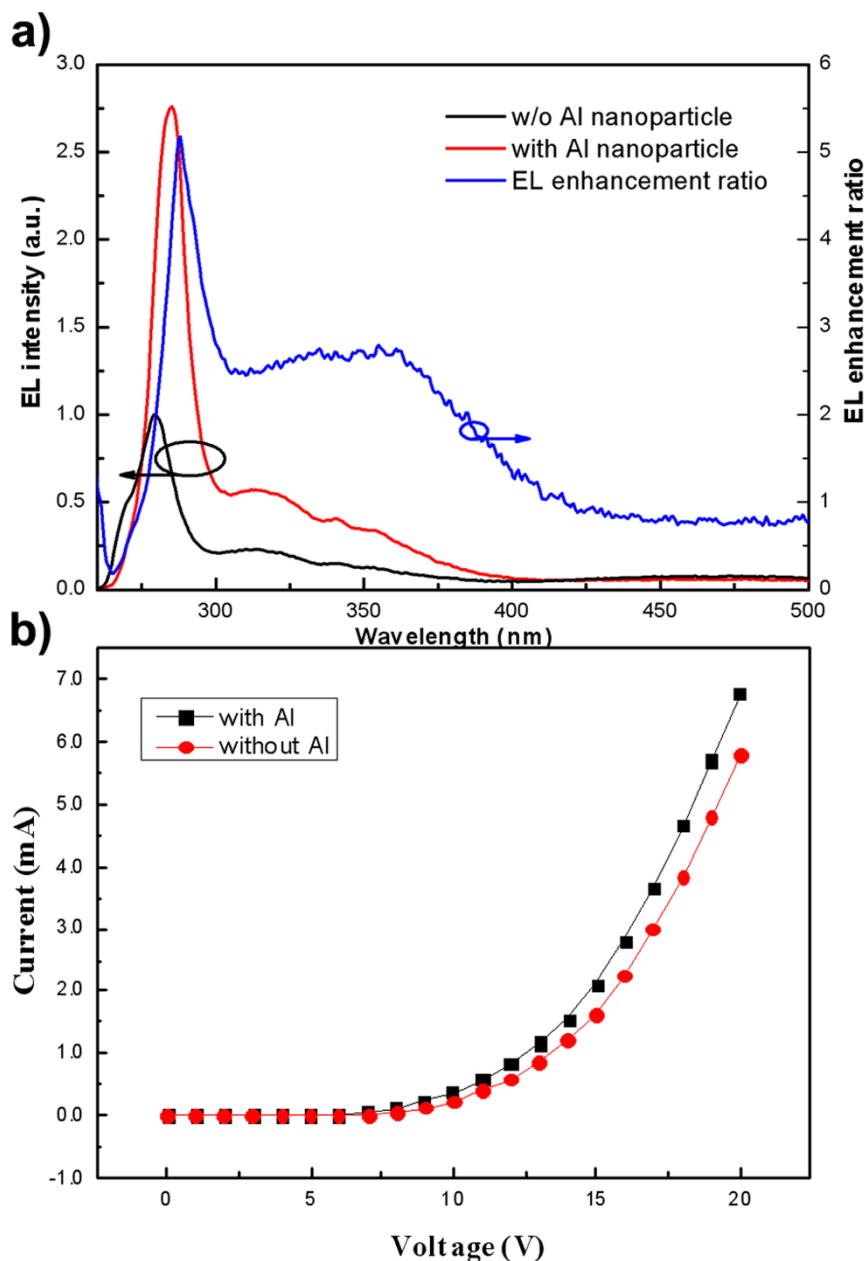


**Figure 5 | Electroluminescence measurements and  $I$ - $V$  curves.** (a) EL spectra of deep-UV LED samples without Al NPs (black line) and with Al NPs deposited on the top surface at  $75^\circ$  (red line) as well as the enhancement ratio between them (blue line). The EL measurement was performed from the bottom side of the LEDs. (b) Current versus applied voltage ( $I$ - $V$  curves) of samples A (black line) and D (red line).

mode I, the radiation fraction directed back into the substrate is greatest at larger angles. In this case, the light directed back into the LEDs would be totally reflected because of the different refractive indices of the LEDs and the sapphire. However, for the radiation patterns of the LSPs of modes II and III, the proportion of radiation close to the normal, which is the centre of the escape cone for the back emission, is much higher than that for mode I. Thus, the light generated by the recombination of the LSPs of modes II and III can be more easily extracted from the back side of the LEDs.

Because of the absorption in the top p-GaN contact layer used in deep-UV LED designs, the bottom emission is the more commonly used light-output structure. Thus, the bottom-emission enhancement is more important than the top-emission enhancement. As seen from Fig. 3b, the ratio of the primary-emission-peak intensity of sample C to that of sample A (at 286 nm and 279 nm, respectively) was approximately 1.36, indicating that the deposition of Al NPs on

the top surface of deep-UV LEDs can improve the bottom emission of the LEDs, although the emission wavelength will exhibit a redshift. For the bottom emission of sample C, the wavelength of the maximum enhancement ratio was approximately 291 nm, which is 12 nm longer than the primary emission wavelength of the MQWs. The theoretical simulation indicated that the wavelength of mode II will blueshift when the size of the cube decreases (Fig. 4c). Thus, we chose the smaller Al NPs, which were deposited at a  $75^\circ$  angle, to further optimise the bottom emission of the deep-UV LEDs.

Figure 5a shows the bottom-emission EL spectra of sample D and sample A and their relative enhancement ratio at an injection current of 15 mA. Compared with sample A, the primary emission wavelength of sample D underwent a redshift to 284 nm. The wavelength of the maximum enhancement ratio was approximately 287 nm, with an enhancement ratio of 5.14. The ratio of the primary-emis-



sion-peak intensity of the LED with Al NPs to that of the LED without Al NPs (at 284 nm and 279 nm, respectively) was approximately 2.75. In comparison with sample C, the wavelength of the maximum enhancement ratio was closer to the primary emission wavelength of the MQWs (8 nm longer). The coupling strength of the mode II LSPs was stronger for sample D than for sample C, which is why the maximum enhancement ratio and the ratio of the primary-emission peak-intensity of the LED with Al NPs to that of the LED without Al NPs were larger for sample D than for sample C.

The current versus the applied voltage ( $I$ - $V$  curves) of samples A and D are shown in Fig. 5b. Sample D exhibited a smaller turn-on and a larger current than sample A at the same voltages. This result is very similar to the results reported by Yeh *et al.*<sup>35</sup>.

## Discussion

In summary, the output power of deep-UV LEDs can be promisingly enhanced when the light waves generated in the MQWs are coupled to LSPs, which were generated on Al NPs on the devices investigated here, for both top- and bottom-emission applications. With an injection current of 15 mA, EL peak-intensity enhancements of up to 6.1-fold for top emission and 1.4-fold for bottom emission were achieved when Al NPs were deposited at a 60° angle. A maximum 10-fold top-emission enhancement at a wavelength of 269 nm and a maximum 2.8-fold bottom-emission enhancement at a wavelength of 291 nm were observed. The difference in the maximum-enhancement wavelengths can be attributed to the substrate-induced Fano resonance effect of the polygonal Al NPs. The bottom-emission LSP enhancement of the deep-UV LEDs was then optimised using smaller Al NPs deposited at a 75° angle. A maximum 5.1-fold bottom-emission EL enhancement at a wavelength of 287 nm was achieved. The emission-peak-intensity enhancement ratio increased from 1.36 to 2.75 when the deposition angle was increased from 60° to 75°. We believe that if the wavelength of the plasmon mode oriented toward the substrate can be brought closer to the primary emission wavelength by regulating the size and shape of the Al NPs, the emission-peak intensity will be further enhanced and exhibit a smaller wavelength shift.

## Methods

**Sample fabrication.** Complete structural deep-UV LED samples were grown on a sapphire (0001) substrate via metal-organic vapour-phase epitaxy (MOVPE) in a vertical Thomas Swan system (3 × 2-inch CCS Aixtron). The sources were trimethylgallium (TMG), trimethylaluminum (TMA), trimethylindium (TMI), and ammonia (NH<sub>3</sub>), and H<sub>2</sub> was used as the carrier gas. Silane (SiH<sub>4</sub>) and bis-cyclopentadienylmagnesium (Cp<sub>2</sub>Mg) were introduced during growth for n-type and p-type doping, respectively. A 1-μm-thick undoped AlN buffer layer and a 1.5-μm n-type Al<sub>0.5</sub>Ga<sub>0.5</sub>N layer were grown on the substrate. An AlGaN MQW array, which consisted of three periods of 5-nm-thick Al<sub>0.35</sub>Ga<sub>0.65</sub>N wells and 10 nm thick Al<sub>0.45</sub>Ga<sub>0.55</sub>N barriers, was subsequently grown. Finally, an 80-nm-thick p-type Al<sub>0.5</sub>Ga<sub>0.5</sub>N layer and a 10-nm p-type GaN capping layer were deposited on the MQWs. Subsequently, a 6-nm-thick Al layer was evaporated on the top of the wafer surfaces by a vacuum electron-beam (E-beam) deposition system (VPT CITATION ITM) using the oblique-angle deposition method to perform PL and SEM measurements. The apparatus used for the oblique-angle deposition has a sample stage with controllable polar-angle rotation, on which the LEDs were loaded. For each sample, the sample stage was held at a fixed polar angle to ensure that the sample was oriented at a certain tilt angle with respect to the vapour-flux direction: 45°, 60°, and 75° for samples B, C, and D, respectively. Prior to the EL measurements, the samples were first subjected to rapid thermal annealing (RTA 300) in an N<sub>2</sub> atmosphere at 850°C for 600 s. Then, the n-type contact was etched 400 nm down to the n-Al<sub>0.5</sub>Ga<sub>0.5</sub>N cladding layer in an n-type mesa structure using the inductively coupled plasma (ICP, Oxford Plasma Lab System 100) technique. Via standard photolithography, E-beam deposition and lift-off processes, Ti/Al/Ti (30/200/5 nm) and Ni (40 nm) were deposited to form n-contact and p-contact electrodes, respectively, which were then annealed at 850°C for 90 s in an N<sub>2</sub> atmosphere and at 400°C for 600 s in an air atmosphere. Finally, Al NPs were evaporated onto the completed LED devices via oblique-angle deposition.

**Measurements.** The surface morphologies of the samples were investigated using a field-emission scanning electron microscopy (SEM, Hitachi S-4800) system. PL measurements were conducted at room temperature by exciting the MQWs with a 248 nm KrF laser. The measurements were performed from the top sides of the LEDs

(Al-NP/epitaxy-layer side). The luminescence was measured using a spectrometer (Avaspec-2048 × 14). EL measurements were performed at room temperature in cw operation mode (TTECH DC SOURCE METER) and measured using a spectrometer (Avaspec-2048 × 14) from the top sides and the bottom sides of the LEDs.

**FDTD simulations.** From careful observation of the SEM images shown in Fig. 1, it is apparent that the Al NPs were polygonal rather than hemispherical. For simplicity, we chose a cube shape to simulate the plasmon modes of the Al NPs. Considering that the penetration depth of the SP fringing field into the semiconductor was approximately 45 nm, which is larger than the thickness of the GaN capping layer, the effective refractive index of the semiconductor layers below the Al NPs should have been a value between the refractive index of GaN and that of Al<sub>0.5</sub>Ga<sub>0.5</sub>N. Thus, the refractive index of the substrate was taken to be 2.4. The side length of the nanocube was chosen to be 16 nm to match the microscope parameters. Unlike noble metals, Al rapidly oxidises when exposed to the atmosphere, forming a thin Al<sub>2</sub>O<sub>3</sub> layer that prevents further attack by oxygen<sup>36</sup>. Thus, the nanocube was defined as a 10 × 10 × 10 nm Al core within a 3-nm alumina shell (Fig. 4a). The incident wave was launched from a box around the NPs to simulate a plane wave propagating from the infinite half-space substrate in the total-field scattered-field formulation with a polarisation parallel to the cube edge.

1. Taniyasu, Y., Kasu, M. & Makimoto, T. An aluminium nitride light-emitting diode with a wavelength of 210 nanometres. *Nature* **441**, 325–328 (2006).
2. Oto, T., Banal, R. G., Kataoka, K., Funato, M. & Kawakami, Y. 100 mW deep-ultraviolet emission from aluminum-nitride-based quantum wells pumped by an electron beam. *Nature Photon.* **4**, 767–770 (2010).
3. Khan, A., Balakrishnan, K. & Katona, T. Ultraviolet light-emitting diodes based on group three nitrides. *Nature Photon.* **2**, 77–84 (2008).
4. Shatalov, M. *et al.* Efficiency of light emission in high aluminum content AlGaN quantum wells. *J. Appl. Phys.* **105**, 073103 (2009).
5. Fujii, T. *et al.* Increase in the extraction efficiency of GaN-based light emitting diodes via surface roughening. *Appl. Phys. Lett.* **84**, 855–857 (2004).
6. Zhang, J., Zhao, H. & Tansu, N. Effect of crystal-field split-off hole and heavy-hole bands crossover on gain characteristics of high Al-content AlGaN quantum well lasers. *Appl. Phys. Lett.* **97**, 111105 (2010).
7. Kolbe, T. *et al.* Effect of temperature and strain on the optical polarization of (In)(Al)GaN ultraviolet light emitting diodes. *Appl. Phys. Lett.* **99**, 261105 (2011).
8. Shakya, J., Kim, K. H., Lin, J. Y. & Jiang, H. X. Enhanced light extraction in III-nitride ultraviolet photonic crystal light-emitting diodes. *Appl. Phys. Lett.* **85**, 142–144 (2004).
9. Wierer, J. J., David, A. & Megens, M. M. III-nitride photonic-crystal light-emitting diodes with high extraction efficiency. *Nature Photon.* **3**, 163–169 (2009).
10. Fan, S., Villeneuve, P., Joannopoulos, J. & Schubert, E. High Extraction Efficiency of Spontaneous Emission from Slabs of Photonic Crystals. *Phys. Rev. Lett.* **78**, 3294–3297 (1997).
11. Bell, A. *et al.* Light emission and microstructure of Mg-doped AlGaN grown on patterned sapphire. *Appl. Phys. Lett.* **82**, 349–351 (2003).
12. Wu, D. S. *et al.* Enhanced Output Power of Near-Ultraviolet InGaN-GaN LEDs Grown on Patterned Sapphire Substrates. *IEEE Photon. Tech. Lett.* **17**, 288–290 (2005).
13. Khizar, M., Fan, Z. Y., Kim, K. H., Lin, J. Y. & Jiang, H. X. Nitride deep-ultraviolet light-emitting diodes with microlens array. *Appl. Phys. Lett.* **86**, 173504 (2005).
14. Lee, M. & Kuo, K. Single-step fabrication of Fresnel microlens array on sapphire substrate of flip-chip gallium nitride light emitting diode by focused ion beam. *Appl. Phys. Lett.* **91**, 051111 (2007).
15. Koo, W. H. *et al.* Light Extraction of Organic Light Emitting Diodes by Defective Hexagonal-Close-Packed Array. *Adv. Funct. Mater.* **22**, 3454–3459 (2012).
16. Nam, K. B., Li, J., Nakarmi, M. L., Lin, J. Y. & Jiang, H. X. Unique optical properties of AlGaN alloys and related ultraviolet emitters. *Appl. Phys. Lett.* **84**, 5264–5266 (2004).
17. Kawanishi, H., Senuma, M., Yamamoto, M., Niikura, E. & Nukui, T. Extremely weak surface emission from (0001) c-plane AlGaN multiple quantum well structure in deep-ultraviolet spectral region. *Appl. Phys. Lett.* **89**, 081121 (2006).
18. Gao, N. *et al.* Surface-plasmon-enhanced deep-UV light emitting diodes based on AlGaN multi-quantum wells. *Sci. Rep.* **2**, 816–819 (2012).
19. Okamoto, K. *et al.* Surface-plasmon-enhanced light emitters based on InGaN quantum wells. *Nature Mater.* **3**, 601–605 (2004).
20. Kwon, M. K. *et al.* Surface-plasmon-enhanced light-emitting diodes. *Adv. Mater.* **20**, 1253–1257 (2008).
21. Maier, S. A. *Plasmonics: Fundamentals and Applications* (Springer, 2007).
22. Chuang, W. H., Wang, J. Y., Yang, C. C. & Kiang, Y. W. Differentiating the contributions between localized surface plasmon and surface plasmon polariton on a one-dimensional metal grating in coupling with a light emitter. *Appl. Phys. Lett.* **92**, 133115 (2008).
23. Willets, K. A. & Van Duyne, R. P. Localized surface plasmon resonance spectroscopy and sensing. *Annu. Rev. Phys. Chem.* **58**, 267–297 (2007).
24. Anker, J. N. *et al.* Biosensing with plasmonic nanosensors. *Nature Mater.* **7**, 442–453 (2008).
25. Ekinci, Y., Salok, H. H. & Löffler, J. F. Plasmon resonances of aluminum nanoparticles and nanorods. *J. Appl. Phys.* **104**, 083107 (2008).



26. Taguchi, A., Saito, Y., Watanabe, K., Song, Y. J. & Kawata, S. Tailoring plasmon resonances in the deep-ultraviolet by size-tunable fabrication of aluminum nanostructures. *Appl. Phys. Lett.* **101**, 081110 (2012).
27. Xi, J. Q. *et al.* Optical thin-film materials with low refractive index for broadband elimination of Fresnel reflection. *Nature Photon.* **1**, 176–179 (2007).
28. Zhang, S. P., Bao, K., Halas, N. H., Xu, H. X. & Nordlander, P. Substrate-induced Fano resonances of a plasmonic nanocube: a route to increased-sensitivity localized surface plasmon resonance sensors revealed. *Nano Lett.* **11**, 1657–1663 (2011).
29. Luk'yanchuk, B. *et al.* The Fano resonance in plasmonic nanostructures and metamaterials. *Nature Mater.* **9**, 707–715 (2010).
30. Miroschnichenko, A. E., Flach, S. & Kivshar, Y. S. Fano resonances in nanoscale structures. *Rev. Mod. Phys.* **82**, 2257–2298 (2010).
31. Cho, C. Y. *et al.* Enhanced optical output power of green light-emitting diodes by surface plasmon of gold nanoparticles. *Appl. Phys. Lett.* **98**, 051106 (2011).
32. Jensen, T. R., Malinsky, M. D., Haynes, C. L. & Van Duyne, R. P. Nanosphere lithography: Tunable localized surface plasmon resonance spectra of silver nanoparticles. *J. Phys. Chem. B* **104**, 10549 (2000).
33. Stockman, M. I. Nanoplasmonics: past, present, and glimpse into future. *Opt. Express* **19**, 22029–22106 (2011).
34. Sherry, L. J. *et al.* Localized surface plasmon resonance spectroscopy of single silver nanocubes. *Nano Lett.* **5**, 2034–2038 (2005).
35. Yeh, D. M., Huang, C. F., Chen, C. Y., Lu, Y. C. & Yang, C. C. Localized surface plasmon-induced emission enhancement of a green light-emitting diode. *Nanotechnology* **19**, 345201 (2008).
36. Chan, G. H., Zhao, J., Schatz, G. C. & Van Duyne, R. P. Localized surface plasmon resonance spectroscopy of triangular aluminum nanoparticles. *J. Phys. Chem. C* **112**, 13958–13963 (2008).

## Acknowledgments

We thank Weihuang Yang, Hangyang Chen, Dayi Liu and Linzhe Cui for their technical assistance. This work was supported by the National Research Program of China under grant Nos. 2011CB301905 and 2012CB619301, the National Natural Science Foundation of China under grant Nos. 61108064, 61227009, 11304257 and 91321102, and the Fundamental Research Funds for the Central Universities (2011120143).

## Author contributions

All authors planned the experiment and discussed the data. The sample was fabricated by N.G., X.C. and X.Y.; the measurement was performed by K.H., N.G., X.C. and J.C.L.; the FDTD simulation was performed by N.G. and C.Z.W.; K.H., N.G., S.P.L. and J.C.L. analysed the data; and K.H., N.G. and J.Y.K. wrote the manuscript.

## Additional information

**Competing financial interests:** The authors declare no competing financial interests.

**How to cite this article:** Huang, K. *et al.* Top- and bottom-emission-enhanced electroluminescence of deep-UV light-emitting diodes induced by localised surface plasmons. *Sci. Rep.* **4**, 4380; DOI:10.1038/srep04380 (2014).



This work is licensed under a Creative Commons Attribution-NonCommercial-ShareAlike 3.0 Unported license. To view a copy of this license, visit <http://creativecommons.org/licenses/by-nc-sa/3.0>